

Twist-angle sensitivity of electron correlations in moiré graphene bilayers

Supplementary Material

Zachary A. H. Goodwin, Fabiano Corsetti, Arash A. Mostofi, and Johannes Lischner
*Departments of Materials and Physics and the Thomas Young Centre for Theory and Simulation of Materials,
 Imperial College London, South Kensington Campus,
 London SW7 2AZ, UK*

(Dated: August 27, 2019)

I. METHODS

A. Atomic structure

The structure of twisted bilayer graphene (tBLG) is generated from AA stacked bilayer graphene by rotating the top graphene sheet around an axis perpendicular to the bilayer that intersects one carbon atom in each layer, producing a structure with D_3 symmetry¹. To obtain a commensurate structure, see Fig. S1(a) for example, an atom of the rotated top layer must reside above an atom of the (unrotated) bottom layer. The corresponding lattice vectors of the moiré unit cell are given by $\mathbf{R}_1 = n\mathbf{a}_1 + m\mathbf{a}_2$ and $\mathbf{R}_2 = -m\mathbf{a}_1 + (n+m)\mathbf{a}_2$, where n and m are integers and $\mathbf{a}_1 = (\sqrt{3}/2, -1/2)a_0$ and $\mathbf{a}_2 = (\sqrt{3}/2, 1/2)a_0$ denote the lattice vectors of graphene with $a_0 = 2.46$ Å being graphene's lattice constant^{1,2}. The twist angle θ can be obtained from n and m via

$$\cos\theta = \frac{n^2 + 4nm + m^2}{2(n^2 + nm + m^2)}. \quad (\text{S1})$$

At small twist angles ($\theta < 10^\circ$), significant lattice relaxations occur in tBLG³⁻⁷. There are both in-plane relaxations, resulting from the growth of the lower-energy AB regions and corresponding shrinkage of AA regions, and large out-of-plane corrugations arising from the different interlayer separations of AB and AA stacked bilayer graphene^{6,7}, see Fig. S1(b). Here, we only take out-of-plane relaxations into account as they have a larger magnitude than in-plane distortions. Specifically, we employ the expression proposed in Ref. 8 for the vertical displacement of carbon atoms at position \mathbf{r} given by

$$z(\mathbf{r}) = d_0 + 2d_1 \sum_i \cos(\mathbf{b}_i \cdot \mathbf{r}). \quad (\text{S2})$$

Here, the summation runs over the primitive reciprocal lattice vectors of tBLG, $\mathbf{b}_{1/2}$, and the sum of these vectors; and $d_0 = (d_{AA} + 2d_{AB})/3$ and $d_1 = (d_{AA} - d_{AB})/9$ with $d_{AB} = 3.35$ Å and $d_{AA} = 3.60$ Å being the interlayer separations of AB and AA stacked bilayer graphene, respectively⁸.

B. Slater-Koster Rules

To calculate the hopping parameters, we employ the Slater-Koster approach^{1,9,10}

$$t(\mathbf{r}) = V_{pp\sigma}(\mathbf{r}) \left(\frac{\mathbf{r} \cdot \mathbf{e}_z}{|\mathbf{r}|} \right)^2 + V_{pp\pi}(\mathbf{r}) \left(1 - \left[\frac{\mathbf{r} \cdot \mathbf{e}_z}{|\mathbf{r}|} \right]^2 \right); \quad (\text{S3})$$

where $V_{pp\sigma}(\mathbf{r}) = V_{pp\sigma}^0 \exp\{q_\sigma(1-|\mathbf{r}|/d_{AB})\}$ and $V_{pp\pi}(\mathbf{r}) = V_{pp\pi}^0 \exp\{q_\pi(1-|\mathbf{r}|/a)\}$ with $V_{pp\sigma}^0 = 0.48$ eV and $V_{pp\pi}^0 = -2.7$ eV⁹⁻¹¹. Note that $a = 1.42$ Å is the carbon-carbon bond length in graphene and $q_\sigma = 7.43$ and $q_\pi = 3.14$ ^{1,2}.

C. Bloch States

The Bloch eigenstates of the tight-binding Hamiltonian are given by

$$\psi_{n\mathbf{k}}(\mathbf{r}) = \frac{1}{\sqrt{N}} \sum_{j\mathbf{R}} c_{jn\mathbf{k}} e^{i\mathbf{k} \cdot \mathbf{R}} \phi_z(\mathbf{r} - \mathbf{t}_j - \mathbf{R}), \quad (\text{S4})$$

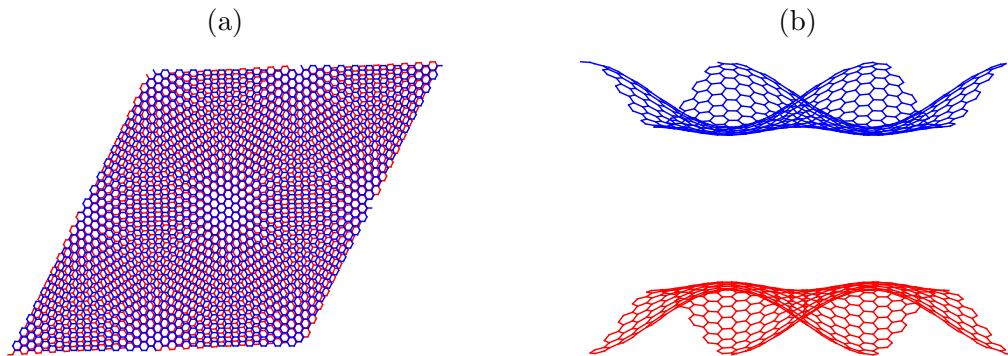


FIG. S1. (a) Moiré lattice of twisted bilayer graphene for a twist angle of 3.15° . (b) Side view of twisted bilayer graphene. Note that the atomic structure was calculated with $d_{AB} = 1 \text{ \AA}$ and $d_{BA} = 2 \text{ \AA}$ with the z-axis expanded for viewing purposes.

where ϕ_z denotes the wavefunction of the p_z -orbital, \mathbf{t}_j is the position of carbon atom j in the unit cell, N denotes the number of moiré unit cells in the crystal and $c_{j\mathbf{n}\mathbf{k}}$ are coefficients obtained from the diagonalization of the Hamiltonian.

D. Wannier Functions

As mentioned in the main text, the four flat bands near the Fermi energy are separated from all other bands by energy gaps in the magic-angle regime. Hence, these bands form a manifold that can be wannierized without a disentanglement procedure¹².

To constrain the Wannier function centres, the selective localization method was employed to calculate two Wannier functions: one centered on the AB position and the other on the BA position of the moiré unit cell^{8,13–15}. We utilise the approach of Wang *et al.*¹⁶ and constrain the centres of two Wannier functions to lie at the AB and BA positions. In this approach, one minimizes the cost function

$$\Omega = \sum_{n=1}^{J'} \left[\langle r^2 \rangle_n - \bar{\mathbf{r}}_n^2 + \lambda(\bar{\mathbf{r}}_n - \mathbf{r}_{0n})^2 \right], \quad (\text{S5})$$

where the first two terms describe the quadratic spread of the Wannier functions (with $\langle r^2 \rangle_n = \langle w_{n\mathbf{R}} | r^2 | w_{n\mathbf{R}} \rangle$ and $\bar{\mathbf{r}}_n = \langle w_{n\mathbf{R}} | \mathbf{r} | w_{n\mathbf{R}} \rangle$ ^{12,17}) and the third term enforces the additional constraint that the centre of the n -th Wannier function should be located at position \mathbf{r}_{0n} ¹⁶. Also, $\lambda = 200$ denotes the cost parameter and we use $J' = 2$.

To calculate maximally localized Wannier functions, a starting guess is required^{12,17}. We constructed two different starting guesses following suggestions from Ref. 13 and Ref. 8, and studied the dependence of the Wannier functions on the initial guess. For the first guess¹³, a linear combination of Bloch states at the Γ -point is constructed and then multiplied by a Gaussian envelope function with an appropriately chosen decay length. For the second guess⁸, the gauge of Bloch states with a given band index was fixed by imposing that the wavefunctions are positive and real at either the AB or the BA positions. Then, the resulting Bloch states were inserted into Eq. (2) of the main text and transformed with $U_{nm}^{\mathbf{k}} = \delta_{nm}$. For both starting points, we determine maximally localized Wannier functions using a $30 \times 30 \times 1$ k-point grid as implemented in the Wannier90 code (version 3.0)¹⁸. We find that the final Wannier functions from the two initial guesses are qualitatively very similar to each other. In Fig. S2, Wannier functions for the initial guess of Ref. 13 can be seen for three twist angles.

1. Input Calculation Details

We are required to calculate $M_{mn}^{\mathbf{k},\mathbf{q}} = \langle u_{m\mathbf{k}} | u_{n\mathbf{k}+\mathbf{q}} \rangle$ for the Wannier90 code¹⁸, where $u_{n\mathbf{k}}$ is the unit cell periodic part of the Bloch state, as seen by $\psi_{n\mathbf{k}} = e^{i\mathbf{k}\cdot\mathbf{r}} u_{n\mathbf{k}}(\mathbf{r})$. Inserting these unit cell periodic functions and shifting coordinate systems with the transformation $\mathbf{r}' = \mathbf{r} - \mathbf{R}$, evaluating a sum and then assuming contributions only come from the overlap of the same orbital, we arrive at

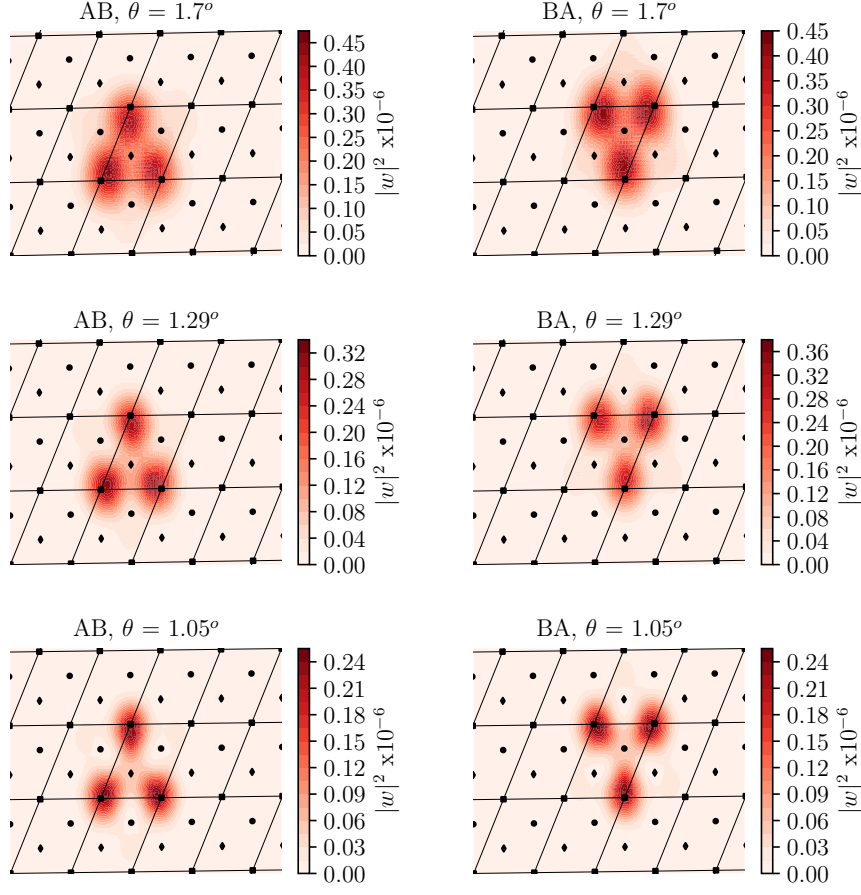


FIG. S2. Calculated Wannier functions centred on AB and BA positions for the three twist angles that were studied for the extended Hubbard parameters.

$$\langle u_{m\mathbf{k}} | u_{n\mathbf{k}+\mathbf{q}} \rangle = \sum_j c_{m\mathbf{k}i}^* c_{n\mathbf{k}+\mathbf{q}i} e^{i\mathbf{q}\mathbf{t}_j} \int d\mathbf{r}'' \phi_z^*(\mathbf{r}'') e^{i\mathbf{q}\mathbf{r}''} \phi_z(\mathbf{r}''), \quad (\text{S6})$$

where $\mathbf{r}'' = \mathbf{r}' - \mathbf{t}_j$.

Here ϕ_z is the pseudo-hydrogenic p_z orbital of carbon atoms. The integral

$$I(\mathbf{q}) = \int d\mathbf{r} \phi_z^*(\mathbf{r}) e^{i\mathbf{q}\mathbf{r}} \phi_z(\mathbf{r}), \quad (\text{S7})$$

can be solved exactly, yielding $I(\mathbf{q}) = [1 + (|\mathbf{q}|a_0/Z)^2]^{-3}$, where a_0 is the Bohr radius and Z is the effective charge of the carbon atom, taken to be 3.18¹⁹.

The initial guess, g_n , is utilised to calculate $A_{mn}^{\mathbf{k}} = \langle \psi_{m\mathbf{k}} | g_n \rangle$ for the Wannier90 code¹⁸. In one of the guesses we fix the gauge of the Bloch state at each \mathbf{k} -point, $\psi_{n\mathbf{k}}$, and separately Fourier transform each state to yield g_n . With this guess, we simply have $A_{mn}^{\mathbf{k}} = \delta_{mn}$.

The other initial guess can be expressed in the form

$$|g_n\rangle = \sum_{n'} \psi_{n'\Gamma}^v(\mathbf{r}) f(\mathbf{r} - \mathbf{r}_0), \quad (\text{S8})$$

where $f(\mathbf{r} - \mathbf{r}_0)$ is a Gaussian function centred at \mathbf{r}_0 and v denotes a sub-lattice and layer of tBLG. Inserting this guess and the Bloch states in a local basis set, we have

$$A_{mn}^{\mathbf{k}} = \frac{1}{N} \sum_{n'} \sum_{\mathbf{R}\mathbf{R}'} \sum_{jv_i} c_{m\mathbf{k}j}^* c_{n'\Gamma v_i} e^{-i\mathbf{k}\cdot\mathbf{R}} \int d\mathbf{r} \phi^*(\mathbf{r} - \mathbf{t}_j - \mathbf{R}) f(\mathbf{r} - \mathbf{r}_0) \phi(\mathbf{r} - \mathbf{t}_{v_i} - \mathbf{R}'). \quad (\text{S9})$$

Note that v_i only runs over the atoms located on the layer and sublattice of v . Let's assume that only non-vanishing contributions come from the same p_z orbital, and that the Gaussian is a slowly varying function, such that it can be taken outside of the integral. After evaluating these operations, we arrive at

$$A_{mn}^{\mathbf{k}} = \frac{1}{N} \sum_{n'} \sum_{\mathbf{R}} \sum_{v_i} c_{m\mathbf{k}v_i}^* c_{n'\Gamma v_i} e^{-i\mathbf{k}\cdot\mathbf{R}} f(\mathbf{t}_{v_i} + \mathbf{R} - \mathbf{r}_0). \quad (\text{S10})$$

This summation over \mathbf{R} is performed over the entire crystal.

E. Coulomb Matrix Elements

To evaluate Eq. (4) of the main text, the Wannier functions are expressed as a linear combination of p_z -orbitals according to

$$w_{n\mathbf{R}}(\mathbf{r}) = \sum_{j\mathbf{R}'} c_{n\mathbf{R}\mathbf{R}'j} \phi_z(\mathbf{r} - \mathbf{t}_j - \mathbf{R}') \quad (\text{S11})$$

with

$$c_{n\mathbf{R}\mathbf{R}'j} = \frac{1}{N} \sum_{m\mathbf{k}} U_{nm}^{(\mathbf{k})} e^{i\mathbf{k}(\mathbf{R}' - \mathbf{R})} c_{m\mathbf{k}j}. \quad (\text{S12})$$

Inserting Eq. (S11) into Eq. (4) of the main text yields

$$V_{n_1\mathbf{R}_1 n_2\mathbf{R}_2} = \sum_{\mathbf{R}'\mathbf{R}''} \sum_{lj} |c_{n_1\mathbf{R}_1 l \mathbf{R}'}|^2 |c_{n_2\mathbf{R}_2 j \mathbf{R}''}|^2 v_{l\mathbf{R}' j \mathbf{R}''}, \quad (\text{S13})$$

where $v_{l\mathbf{R}' j \mathbf{R}''}$ denotes the Coulomb matrix elements between pairs of p_z -orbitals at positions $\mathbf{t}_l + \mathbf{R}'$ and $\mathbf{t}_j + \mathbf{R}''$, respectively. For in-plane separations larger than nearest neighbor distance, we assume $v_{l\mathbf{R}' j \mathbf{R}''} = W(\mathbf{t}_l + \mathbf{R}' - [\mathbf{t}_j + \mathbf{R}''])$. For the on-site ($v_{00} = 17$ eV) and nearest neighbour ($v_{01} = 8.5$ eV) terms, we used values obtained from *ab initio* DFT calculations²⁰. Eq. (S13) is evaluated by explicitly carrying out the summations in real space using a 5×5 supercell which yields highly converged results. While evaluating $v_{l\mathbf{R}' j \mathbf{R}''}$ is straightforward for the Coulomb interaction screened by a semiconducting substrate, the case of a metallic gate is more difficult. Here, we evaluate Eq. (5) of the Main text by summing contributions up to $n = 8$ which was found to reasonably reproduce the fully converged potential well for distances smaller than 40 Å. For larger distances, we employ the analytical long-distance limit of W^g , see discussion following Eq. (5) of the main text. These approximations result in errors of less than five percent in the Hubbard parameters.

II. ON-SITE HUBBARD PARAMETERS

The following labels are used throughout this section to refer to different initial guesses and centres of the Wannier functions.

- (1) - Initial guess from Ref. 8 centred on AB position
- (2) - Initial guess from Ref. 8 centred on BA position
- (3) - Initial guess from Ref. 13 centred on AB position
- (4) - Initial guess from Ref. 13 centred on BA position

(n,m)	θ / degree	(1)	(2)	(3)	(4)
(15,16)	2.13	418.9	415.6	414.5	417.0
(19,20)	1.70	339.8	336.3	329.4	330.1
(21,22)	1.54	310.3	308.1	313.8	312.0
(23,24)	1.41	283.3	283.7	291.2	285.4
(25,26)	1.29	260.6	267.7	260.3	260.8
(26,27)	1.25	249.1	247.8	253.3	250.6
(27,28)	1.20	234.2	232.6	249.2	249.2
(28,29)	1.16	232.4	236.9	237.4	237.6
(29,30)	1.12	224.5	224.0	229.3	225.8
(31,32)	1.05	201.8	206.9	210.7	210.3

TABLE I. On-site Hubbard parameters, in units of meV, calculated from a Coulomb potential with $\epsilon_r = 1$.

(n,m)	θ / degree	(1)	(2)	(3)	(4)
(15,16)	2.13	258.4	255.4	254.2	256.6
(19,20)	1.70	188.1	185.0	179.1	179.6
(21,22)	1.54	163.7	161.5	164.1	159.2
(23,24)	1.41	142.0	142.1	148.6	143.4
(25,26)	1.29	124.6	129.9	122.8	123.4
(26,27)	1.25	116.1	115.4	123.6	116.6
(27,28)	1.20	105.8	105.1	116.5	116.5
(28,29)	1.16	104.8	107.9	108.3	108.5
(29,30)	1.12	99.7	99.0	102.8	100.2
(31,32)	1.05	85.7	88.6	90.9	90.7

TABLE II. On-site Hubbard parameters, in units of meV, calculated in the presence of a metallic gate with $\epsilon_r = 1$.

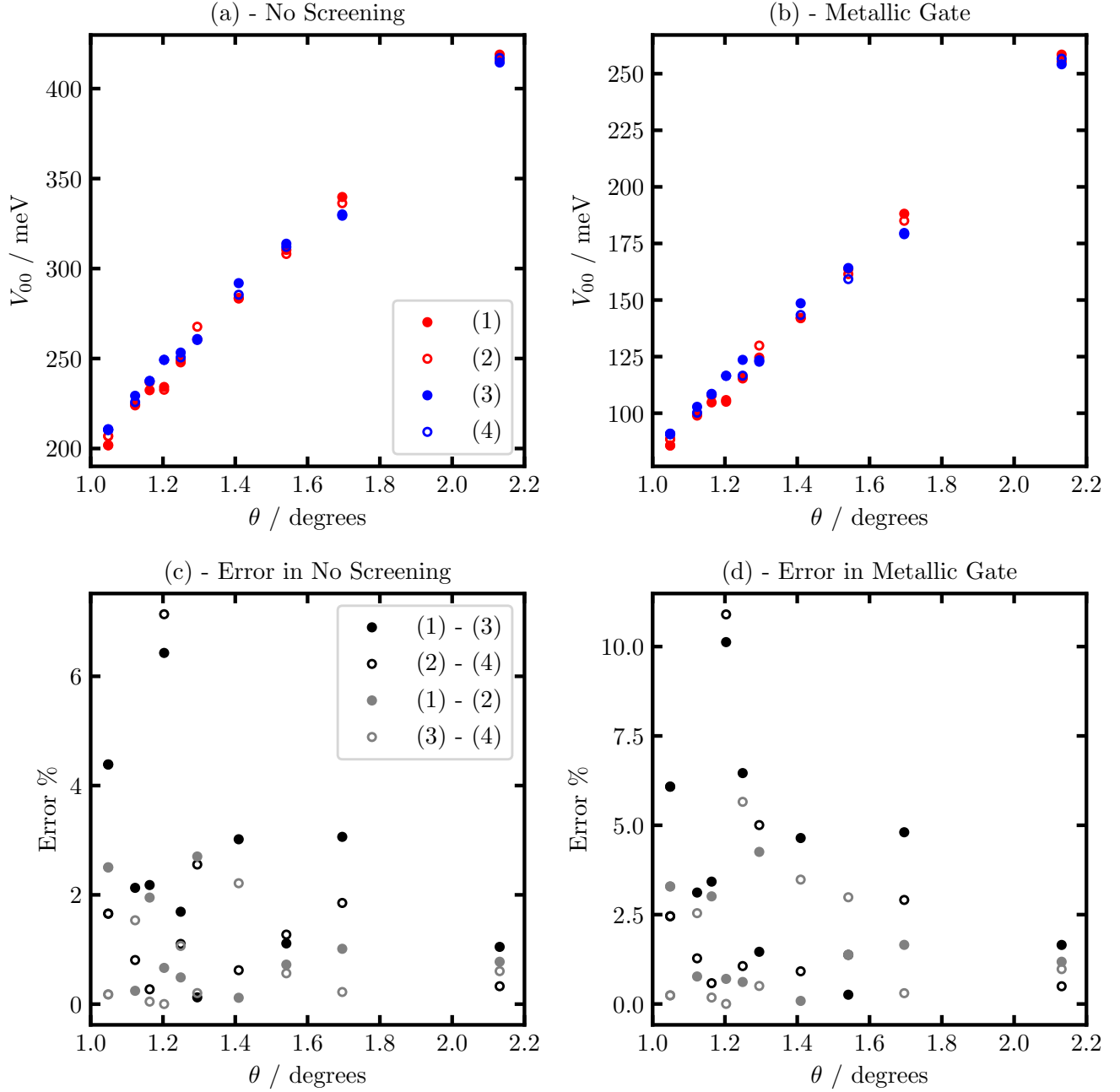


FIG. S3. For (a) and (b), the different symbols and colours represent different initial guesses as inputs for the selective localisation method of wannier90 (V3.0)¹⁸. For details of these see the start of this section. For (c) and (d) there are two numbers for each symbol. These refer to the percentage difference between these two initial guesses from (a) and (b), respectively. (a) - On-site Hubbard parameter as a function of twist angle calculated with Coulomb interaction and $\epsilon_r = 1$. (b) - On-site Hubbard parameter as a function of twist angle calculated in the presence of a metallic gate and $\epsilon_r = 1$. (c) - Percentage errors between on-site Hubbard parameters at each twist angle for (a). (d) - Percentage errors between on-site Hubbard parameters at each twist angle for (b).

Initial Guess	m_{00} / meV/degree	c_{00} / meV
(1)	198.8	-
	198.8	-0.1
(2)	198.8	-
	192.0	9.7
(3)	200.4	-
	184.0	24
(4)	199.8	-
	187.1	18.6

TABLE III. Gradients and intercepts from linear fits of the on-site Hubbard parameters calculated from a Coulomb potential with $\epsilon_r = 1$. Top line of each initial guess is fitted with a line forced through the origin; while the second line is fitted with a free intercept.

Initial Guess	m_{00}^g / meV/degree	c_{00}^g / meV
(1)	103.0	-
	159.5	-82.1
(2)	102.8	-
	154.0	-74.5
(3)	104.0	-
	147.1	-62.8
(4)	103.0	-
	145.0	-68.4

TABLE IV. Gradients and intercepts from linear fits of the on-site Hubbard parameters calculated in the presence of a metallic gate with $\epsilon_r = 1$. Top line of each initial guess is fitted with a line forced through the origin; while the second line is fitted with a free intercept.

III. EXTENDED HUBBARD PARAMETERS

All of the initial guesses for the extended Hubbard parameters were from Ref. 13. All extended Hubbard parameters were calculated by displacing the first Wannier function along one of the lattice vectors of the system (either \mathbf{t}_1 or \mathbf{t}_2 , but not a combination of both). There was always an integer, from 1 to 5, multiply the lattice vector.

- (1) - Interaction from the same AB position along \mathbf{t}_1
- (2) - Interaction from the same BA position along \mathbf{t}_1
- (3) - Interaction from the same AB position along \mathbf{t}_2
- (4) - Interaction from the same BA position along \mathbf{t}_2
- (5) - Interaction between AB and BA position along \mathbf{t}_1
- (6) - Interaction between BA and AB position along \mathbf{t}_1
- (7) - Interaction between AB and BA position along \mathbf{t}_2
- (8) - Interaction between BA and AB position along \mathbf{t}_2

By comparing (1) and (2), for example, the similarity between the two calculated Wannier functions can be determined. The extended Hubbard parameters calculated from these different locations should be identical^{8,13}, but because two Wannier functions were selectively localised with constrained centres, there are small differences between the values of the parameters.

A. Extended Hubbard Parameters - (19,20)

$r / \text{\AA}$	(1)	(2)	(3)	(4)	(5)	(6)	(7)	(8)
48.0	-	-	-	-	272.6	-	274.1	-
83.1	200.3	202.1	205.3	200.8	-	-	-	-
127.0	-	-	-	-	126.8	127.6	127.6	129.3
166.2	92.7	93.0	94.6	92.8	-	-	-	-
209.1	-	-	-	-	71.6	71.7	71.8	72.2
249.3	59.3	59.4	59.7	59.3	-	-	-	-
291.8	-	-	-	-	50.2	50.3	50.3	50.4
332.4	44.0	44.0	44.1	43.9	-	-	-	-
374.7	-	-	-	-	38.8	38.9	38.9	38.9
415.5	35.0	35.0	35.0	25.0	-	-	-	-
457.6	-	-	-	-	-	31.7	-	31.7

TABLE V. On-site Hubbard parameters, in units of meV, calculated from a Coulomb potential with $\epsilon_r = 1$ for a twist angle of 1.70° .

$r / \text{\AA}$	(1)	(2)	(3)	(4)	(5)	(6)	(7)	(8)
48.0	-	-	-	-	131.0	-	132.4	-
83.1	73.7	75.3	78.2	74.1	-	-	-	-
127.0	-	-	-	-	22.5	23.2	23.2	24.6
166.2	6.9	7.0	8.0	6.9	-	-	-	-
209.1	-	-	-	-	1.7	1.8	1.8	2.0
249.3	4.7×10^{-1}	4.7×10^{-1}	5.5×10^{-1}	4.7×10^{-1}	-	-	-	-
291.8	-	-	-	-	1.1×10^{-1}	1.2×10^{-1}	1.1×10^{-1}	1.4×10^{-1}
332.4	3.0×10^{-2}	3.1×10^{-2}	3.5×10^{-2}	3.0×10^{-2}	-	-	-	-
374.7	-	-	-	-	7.3×10^{-3}	8.1×10^{-3}	7.4×10^{-3}	9.0×10^{-3}
415.5	2.0×10^{-3}	2.0×10^{-3}	2.3×10^{-3}	2.0×10^{-3}	-	-	-	-
457.6	-	-	-	-	-	5.4×10^{-4}	-	6.0×10^{-4}

TABLE VI. On-site Hubbard parameters, in units of meV, calculated with account of metallic gate with $\epsilon_r = 1$ for a twist angle of 1.70° .

B. Extended Hubbard Parameters - (25,26)

$r / \text{\AA}$	(1)	(2)	(3)	(4)	(5)	(6)	(7)	(8)
62.7	-	-	-	-	216.5	-	213.7	-
108.6	156.7	157.0	159.1	159.1	-	-	-	-
166.0	-	-	-	-	96.3	97.2	97.5	98.5
217.3	71.1	71.2	72.0	71.6	-	-	-	-
273.4	-	-	-	-	54.6	54.9	54.9	55.2
326.0	45.4	45.4	45.6	45.5	-	-	-	-
381.6	-	-	-	-	38.4	38.5	38.5	38.6
434.6	33.6	33.6	33.7	33.6	-	-	-	-
490.0	-	-	-	-	29.7	29.7	29.7	29.8
543.3	26.7	26.7	26.8	26.8	-	-	-	-
598.4	-	-	-	-	-	24.2	-	24.3

TABLE VII. On-site Hubbard parameters, in units of meV, calculated from a Coulomb potential with $\epsilon_r = 1$ for a twist angle of 1.29° .

$r / \text{\AA}$	(1)	(2)	(3)	(4)	(5)	(6)	(7)	(8)
62.7	-	-	-	-	90.8	-	87.4	-
108.6	48.2	48.2	50.2	50.1	-	-	-	-
166.0	-	-	-	-	11.0	12.2	12.1	13.0
217.3	3.1	3.1	3.6	3.3	-	-	-	-
273.4	-	-	-	-	4.9×10^{-1}	6.6×10^{-1}	6.0×10^{-1}	7.2×10^{-1}
326.0	1.2×10^{-1}	1.2×10^{-1}	1.5×10^{-1}	1.3×10^{-1}	-	-	-	-
381.6	-	-	-	-	1.6×10^{-2}	2.7×10^{-2}	2.0×10^{-2}	3.0×10^{-2}
434.6	3.9×10^{-3}	4.0×10^{-3}	4.8×10^{-3}	4.1×10^{-3}	-	-	-	-
490.0	-	-	-	-	4.8×10^{-4}	8.9×10^{-4}	6.0×10^{-4}	9.6×10^{-4}
543.3	1.2×10^{-4}	1.2×10^{-4}	1.5×10^{-4}	1.2×10^{-4}	-	-	-	-
598.4	-	-	-	-	-	2.8×10^{-5}	-	3.0×10^{-5}

TABLE VIII. On-site Hubbard parameters, in units of meV, calculated with account of metallic gate with $\epsilon_r = 1$ for a twist angle of 1.29° .

C. Extended Hubbard Parameters - (31,32)

$r / \text{\AA}$	(1)	(2)	(3)	(4)	(5)	(6)	(7)	(8)
77.5	-	-	-	-	173.4	-	173.1	-
134.2	128.4	128.3	128.2	128.3	-	-	-	-
205.0	-	-	-	-	78.1	78.3	78.0	78.2
268.4	58.5	58.5	58.4	58.4	-	-	-	-
337.8	-	-	-	-	44.8	44.9	44.6	44.9
402.7	37.0	37.0	37.0	37.0	-	-	-	-
471.4	-	-	-	-	31.2	31.3	31.2	31.3
536.9	27.3	27.3	27.3	27.3	-	-	-	-
605.2	-	-	-	-	24.1	24.1	24.1	24.1
671.1	21.7	21.7	21.7	21.7	-	-	-	-
739.2	-	-	-	-	-	19.7	-	19.7

TABLE IX. On-site Hubbard parameters, in units of meV, calculated from a Coulomb potential with $\epsilon_r = 1$ for a twist angle of 1.05° .

$r / \text{\AA}$	(1)	(2)	(3)	(4)	(5)	(6)	(7)	(8)
77.5	-	-	-	-	64.3	-	64.0	-
134.2	35.3	35.3	35.2	25.4	-	-	-	-
205.0	-	-	-	-	7.2	7.2	7.1	7.2
268.4	2.3	2.3	2.3	2.3	-	-	-	-
337.8	-	-	-	-	4.6×10^{-1}	5.6×10^{-1}	4.5×10^{-1}	5.6×10^{-1}
402.7	1.4×10^{-1}	1.4×10^{-1}	1.3×10^{-1}	1.4×10^{-1}	-	-	-	-
471.4	-	-	-	-	1.4×10^{-2}	3.9×10^{-2}	1.3×10^{-2}	4.0×10^{-2}
536.9	4.2×10^{-3}	4.3×10^{-3}	4.2×10^{-3}	4.2×10^{-3}	-	-	-	-
605.2	-	-	-	-	3.6×10^{-4}	1.3×10^{-3}	3.4×10^{-4}	1.4×10^{-3}
671.1	1.2×10^{-4}	1.2×10^{-4}	1.1×10^{-4}	1.2×10^{-4}	-	-	-	-
739.2	-	-	-	-	-	4.0×10^{-5}	-	4.1×10^{-5}

TABLE X. On-site Hubbard parameters, in units of meV, calculated with account of metallic gate with $\epsilon_r = 1$ for a twist angle of 1.05° .

-
- ¹ G. T. de Laissardière, D. Mayou, and L. Magaud, *Nano Lett.* **10**, 804 (2010).
- ² G. T. de Laissardière, D. Mayou, and L. Magaud, *Phys. Rev. B* **86**, 125413 (2012).
- ³ K. Uchida, S. Furuya, J.-I. Iwata, and A. Oshiyama, *Phys. Rev. B* **90**, 155451 (2014).
- ⁴ A. Oshiyama, J.-I. Iwata, K. Uchida, and Y.-I. Matsushita, *J. Appl. Phys.* **117**, 112811 (2015).
- ⁵ S. Carr, S. Fang, P. Jarillo-Herrero, and E. Kaxiras, *Phys. Rev. B* **98**, 085144 (2018).
- ⁶ F. Gargiulo and O. V. Yazyev, *2D Mater.* **5**, 015019 (2018).
- ⁷ S. K. Jain, V. Juričić, and G. T. Barkema, *2D Mater.* **4**, 015018 (2017).
- ⁸ M. Koshino, N. F. Q. Yuan, T. Koretsune, M. Ochi, K. Kuroki, and L. Fu, *Phys. Rev. X* **8**, 031087 (2018).
- ⁹ J. C. Slater and G. F. Koster, *Phys. Rev.* **94**, 1498 (1954).
- ¹⁰ F. Corsetti, A. A. Mostofi, and J. Lischner, *2D Mater.* **4**, 025070 (2017).
- ¹¹ A. H. C. Neto, F. Guinea, N. M. R. Peres, K. S. Novoselov, and A. K. Geim, *Rev. Mod. Phys.* **81**, 109 (2009).
- ¹² N. Marzari, A. A. Mostofi, J. R. Yates, I. Souza, and D. Vanderbilt, *Rev. Mod. Phys.* **84**, 1419 (2012).
- ¹³ J. Kang and O. Vafek, *Phys. Rev. X* **8**, 031088 (2018).
- ¹⁴ H. C. Po, L. Zou, A. Vishwanath, and T. Senthil, *Phys. Rev. X* **8**, 031089 (2018).
- ¹⁵ N. F. Q. Yuan and L. Fu, *Phys. Rev. B* **98**, 045103 (2018).
- ¹⁶ R. Wang, E. A. Lazar, H. Park, A. J. Millis, and C. A. Marianetti, *Phys. Rev. B* **90**, 165125 (2014).
- ¹⁷ N. Marzari and D. Vanderbilt, *Phys. Rev. B* **56**, 12847 (1997).
- ¹⁸ G. Pizzi, V. Vitale, R. Arita, S. Blügel, F. Freimuth, G. Géranton, M. Gibertini, D. Gresch, C. Johnson, T. Koretsune, J. I. nez Azpiroz, H. Lee, D. Marchand, A. Marrazzo, Y. Mokrousov, J. I. Mustafa, Y. Nohara, Y. Nomura, L. Paulatto, S. Poncè, T. Ponweiser, J. Qiao, F. Thöle, S. Tsirkin, M. Wierzbowska, N. Marzari, D. Vanderbilt, I. Souza, A. A. Mostofi, and J. R. Yates, arXiv:1907.09788v1, www.wannier90.org (2019).
- ¹⁹ K. W.-K. Shung, *Phys. Rev. B* **34**, 979 (1986).
- ²⁰ T. O. Wehling, E. Şaşoğlu, C. Friedrich, A. I. Lichtenstein, M. I. Katsnelson, and S. Blügel, *Phys. Rev. Lett.* **106**, 236805 (2011).